



## Particle tracking and energy loss measurements with the LCTPC: A comparison to simulation models

P. Christiansen, P. Gros, L. Jönsson, M. Ljunggren, B. Lundberg, U. Mjörnmark,  
A. Oskarsson, E. Stenlund, L. Österman

Lund University, Lund, Sweden

K. Fujii, R. Yonamine

KEK, IPNS, Tsukuba, Japan

20.12.2010

### Abstract

The large prototype TPC (LCTPC), instrumented with GEM readout and front-end electronics based on the ALICE ALTRO chip was tested at the DESY T24 electron beam. Data was collected with and without an external magnetic field of 1T, and in both the standard configuration where the tracks are along the long edge (5.2 mm) of the pads and in a perpendicular configuration where the tracks are along the short edge (1.2 mm) of the pads. For electrons with momentum  $p = 5 \text{ GeV}/c$  the straggling function (charge distribution), the specific energy loss ( $dE/dx$ ), and the spatial resolution was extracted and compared to simulations based on GEANT4 energy loss calculations.

The specific energy loss resolution was in general found to be better in the simulation than in the data, due to a narrower straggling function, raising questions about the energy loss modelling of shell effects.

The spatial resolution was found to be well described by the simulations when there was no magnetic field. For magnetic field runs the large  $E \times B$  effect due to inhomogeneities in the electric field, caused by the support structure of the GEMs, is found to deteriorate the resolution from 70  $\mu\text{m}$  to 100  $\mu\text{m}$  even when an average correction is applied. This suggests that a redesign of the GEMs would significantly improve the spatial resolution.

# 1 Introduction

A possible TPC for the ILC has strict performance requirements based on the requirement for the Higgs mass to be determined from the Higgs strahlung processes. The requirement on transverse momentum resolution corresponds to a spatial resolution of better than  $100 \mu m$  at the magnetic field of 4 T.

A broad test beam programs has been carried out within the EUDET framework using a large prototype TPC (LCTPC) with different readout technologies.

In the study presented here the main focus has been on comparing the performance obtained in the test beam measurements to the performance expected from state of the art simulations based on GEANT4 energy loss calculations. The goal of this study is primarily to understand if the performance of the LCTPC is optimal or if it can be further improved, but secondarily it addresses the physics question of to what precision the performance can be simulated.

The note is organised as follows. In section 2-6 the test setup and the detector is described in detail. In section 7-11 the simulation, data analysis, and results are presented. Finally the conclusions of this study are given in section 12.

## 2 The test beam

The measurements were performed at the test beam T24 from the DESY II electron synchrotron [1]. The circulating bunches of electrons are guided towards an internal carbon fibre target to produce bremsstrahlung photons in the energy range up to 7 GeV. The so produced photons are forced to hit an external metal plate to generate electron-positron pairs. Behind the conversion target a dipole magnet causes the electrons and positrons to spread out in the horizontal plane according to their momenta. A collimator cuts out a narrow momentum slice of particles which pass through the collimator. Thus by setting the magnetic field strength, particles with a certain momentum can be selected whereas the energy spread of the electron beam is given by the opening slit of the collimator. A schematic picture of the set-up is shown in Fig. 1.

A telescope of four  $3 \times 3 \text{ cm}^2$  scintillators with a thickness of  $3 \text{ mm}$ , organised in overlapping pairs at a distance of  $\sim 100 \text{ cm}$  between the pairs, provide a beam trigger [2] in a fourfold coincidence.

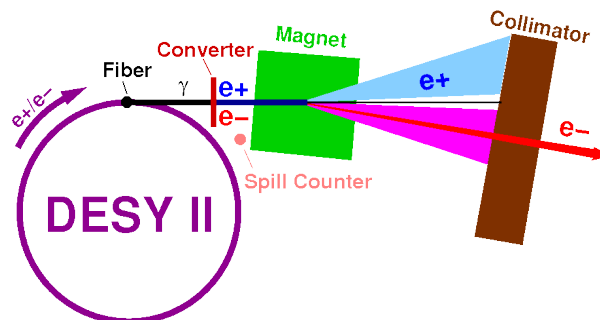


Figure 1: A schematic view of the test beam set-up

## 3 The large prototype TPC

### 3.1 The field cage

The large prototype TPC (LPTPC) [3, 4, 5, 6] consists of a cylindrical field cage and two end caps of which the anode side can be instrumented with various readout systems and the other end contains the cathode. Thus, it is essentially half a normal TPC. The inner diameter of the field cage is  $730\text{ mm}$  and is limited by the core of the superconducting magnet (PCMAG) in which it is housed. The length is limited to  $600\text{ mm}$  by the homogeneity of the magnetic field, which should not vary more than 3% over the length of the drift space. The field cage is constructed out of composite material. The cylinder is made of a  $23.5\text{ mm}$  thick aramid honeycomb wall, which is glued between two layers of glass-fibre reinforced plastic (GRP) and a polyimide layer for electrical insulation. This structure provides the necessary stiffness to prevent significant deformations and presents a minimum of material ( $\sim 1\%$  of  $X_0$ ) with which the particles may interact. The field cage should be able to stand an overpressure from the drift gas of up to  $10\text{ mbar}$ . The inhomogeneity of the drift field should not exceed  $10^{-4}$  over the drift volume and in order to meet this requirement the electrical field is provided by a series of field strips on decreasing potential from the anode to the cathode. These are  $35\text{ }\mu\text{m}$  thick copper strips on both sides of a  $75\text{ }\mu\text{m}$  thick kapton foil, which is glued to the inside of the field cage. The copper strips on the outside are so called mirror strips which are placed to cover the gaps between the field strips, overlapping half a strip width with the inner field strips and are on intermediate potentials. This arrangement of strips provides a homogeneous field to the order which is required. The strips are connected via a resistor chain which distributes the voltage along the drift length with the last strip (counted from the anode) on the same potential as the cathode. The potential of the cathode is about  $-14.5\text{ kV}$  giving a drift field of  $230\text{ V/cm}$ . A schematic view of the field cage and a cross section of the cylinder wall is shown in Fig. 2.

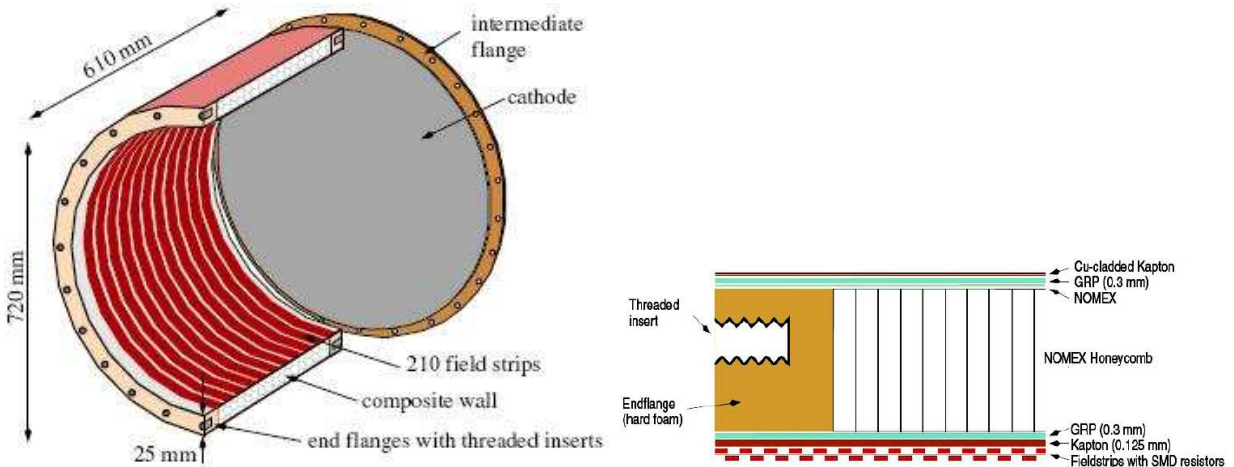


Figure 2: Left side: A schematic drawing of the field cage. Right side: A cross section of the chamber wall.

### 3.2 The end plate

The anode end plate is made from aluminium and the design is such that it should be able to accommodate seven gas amplification modules arranged in a way that corresponds to a subsection of the full scale TPC for the ILC. The accuracy for the insertion of the modules is better than  $50\text{ }\mu\text{m}$ . A picture of the end plate is shown in Fig. 3.

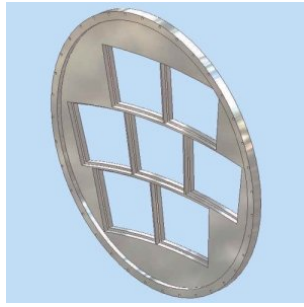


Figure 3: The end plate with the seven mounting positions for the readout chambers

## 4 The GEMs and pad plane

For this measurement, readout chambers based on gas electron multipliers (GEMs) developed by the Asian groups [7, 8] were used and 3200 pads were equipped with the ALTRO readout electronics. The GEM module has a keystone shape with the width of about 23 cm and the height of about 17 cm. The pad board has 5152 pads in total, arranged in 28 rows of about 1 mm wide pads separated by 0.1 mm. The length of the pads is 5.26 mm. The innermost 14 rows have 176 pads/row whereas the outermost 14 rows have 192 pads/row. Due to the shape of the module the width of the pads is increasing with its radial position so that the pad width varies between 1.15 mm and 1.25 mm. The pads of neighbouring rows are staggered with respect to each other by half a pad width. A picture of the pad plane is seen to the right of Fig. 4.

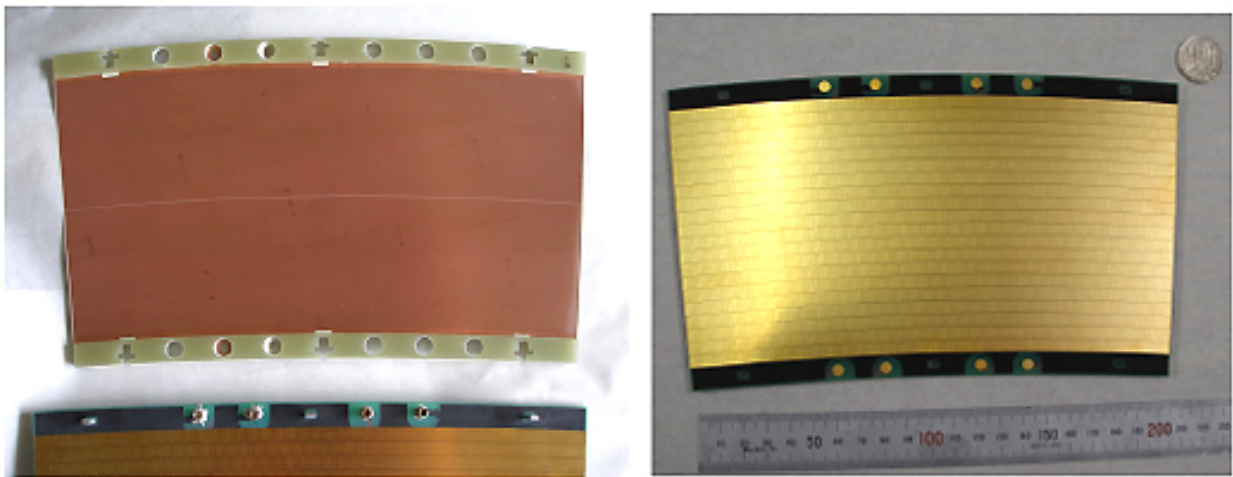


Figure 4: Left side: A GEM plane. Right side: The pad plane. The holes are for support pillars and HV supply.

The GEM modules have two copper layers of 5  $\mu\text{m}$  on each side of a 100  $\mu\text{m}$  thick liquid crystal polymer insulator. The holes are 70  $\mu\text{m}$  in diameter and the pitch between the holes is 140  $\mu\text{m}$ . A picture of a GEM plane is shown to the left of Fig. 4. The GEM system included two layers of GEMs in this test. The GEM foils are supported by two thin G10 frames along the long sides of the pad board and the GEM, respectively. The short sides have no support, which minimises dead regions between the GEMs in the  $\phi$  direction. The distance between the two GEM foils (the transfer gap) and the distance between the last GEM and the pad plane (the induction gap) is 4 mm and 2 mm, respectively.

Since the short sides of the GEM foil have no support, metallic pillars were glued onto the long sides of the pad board, the purpose of which is to keep the GEM foils stretched and in position. Thus,

in the GEM foils and the G10 frames there are corresponding holes into which the pillars fit. An assembled module is shown in Fig. 5. A thin gating GEM was planned to prevent ions to drift back into the drift volume but was not installed at the time of the measurement. The voltage across the thick GEMs was 350 V giving a gas amplification of  $10^4$  for the double GEM system.

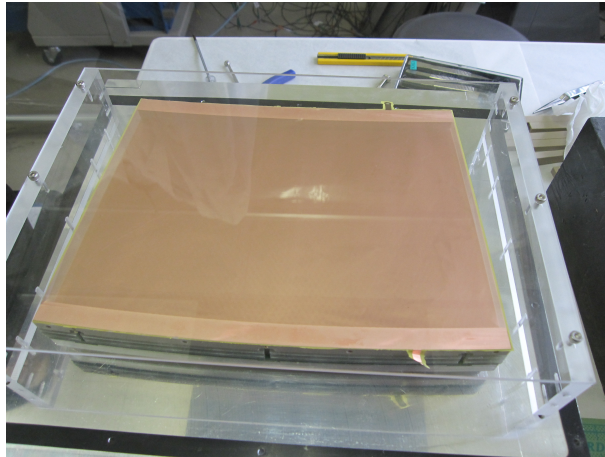


Figure 5: The assembled GEM module

The outermost GEM plane has to be on the same potential as the corresponding strip on that level in order not to cause any inhomogeneities in the drift field. For the Asian GEM module the outermost GEM should have been the gating grid on the level of the seventh strip in the field cage. However, due to the missing gating GEM this had to be accounted for in setting the potentials.

Unfortunately, since the gating grid was never introduced for this measurement, the metallic support pillars were sticking out unshielded, causing deformations of the electric field. This caused a straight track to become bent, where the magnitude of deformation depends on the distance of the track from the pillars. An example of such a reconstructed track is given in Fig. 9.

## 5 The superconducting magnet

The superconducting magnet (PCMAG) [9], which houses the LCTPC, was constructed by Japanese groups originally for the BESS-Polar balloon experiment to study cosmic anti-matter and has therefore a coil of low mass and no return yoke. A technical drawing of the magnet, with the position of the TPC indicated, is shown in Fig. 6.

The diameter of the magnet core is 85 cm and the length inside the magnet, with this diameter, is about 130 cm. The magnet can provide a field of 1.2 T but was in this measurement run at 1 T. The field is, however, not homogeneous over the full length of the magnet due to the non existing return yoke. Only in a region of  $\pm 30$  cm around the centre it is homogeneous to within 3% and this limits the length of the TPC to about 60 cm.

The PCMAG was at the time of these measurement sitting in a fixed position with the beam entering in the centre of the magnetic field so that the influence of the inhomogeneous regions of the field should have a small influence. The only way to measure at different drift lengths was to move the TPC inside the magnet. This is not causing any problems as long as the TPC is pushed further in to the magnet, corresponding to shorter drift lengths, but when the TPC is pulled further out the readout system is entering into the regions of inhomogeneous fields more and more. These measurements were performed at drift lengths in the range of 70 to 300 mm.

## 6 The readout electronics

The readout system for the LCTPC is based on the ALTRO chip [10], originally developed for the ALICE experiment at the LHC. The 16 channel ALTRO chip performs analogue to digital conversion with 10 bit precision followed by various steps of digital signal processing, including zero suppression and storage in an event buffer. The sampling can be clocked at frequencies up to 40  $MHz$  so in principle sampling at this frequency and frequencies lower by multiples of two is possible. However, at 40  $MHz$  sampling the full resolution is not maintained for the standard ALTRO chip. A limited number of ALTRO chips were modified to allow sampling at 40  $MHz$  with almost full precision [11]. Up to now the system has been operated during data taking at 20  $MHz$  only. The ALTRO chip has an event storage memory of 1 k 10-bit words, which corresponds to sampled data over a depth of 50  $\mu s$  drift time at 20  $MHz$  sampling frequency. The so called T2K gas mixture (95/3/2 % Ar/CF<sub>4</sub>/Isobutan) was used in the TPC, which gives a drift velocity of around 7  $cm/\mu s$  at a drift field of 230  $V/cm$ . This leads to a maximum drift length of 350  $cm$  that can be accommodated in the ALTRO memory i.e. much longer than the total length of the LCTPC of 60  $cm$ .

In order to test recent technologies for gas amplification (GEMs and Micromegas for TPC readout) a new charge sensitive preamp-shaper has been developed. The programmable PCA16 chip [12] has, as the name indicates, 16 channels and offers different choices with respect to shaping time, gain, decay time and signal polarity. The new analogue chip required modifications to the Front End Card (FEC), compared to its original design for the ALICE TPC. These are mainly related to the programmability of the PCA16 chip which is done remotely. Data for setting the parameter values are downloaded to the board controller FPGA on the FEC via the data bus on the back plane. An 8-bit shift register delivers the digital input to set the peaking time, the gain, the polarity (common to the 8 PCA16 on a FEC) and it also provides a possibility to bypass the shaping function. An octal DAC (Digital to Analogue Converter) controls the decay time of the preamplifier. The various options will make it possible to find the optimal parameter setting for a certain gas amplification system so that the specifications for the final chip production can be quantified.

Each FEC contains 128 channels i.e. 8 PCA16 chips and 8 ALTRO chips are mounted on each

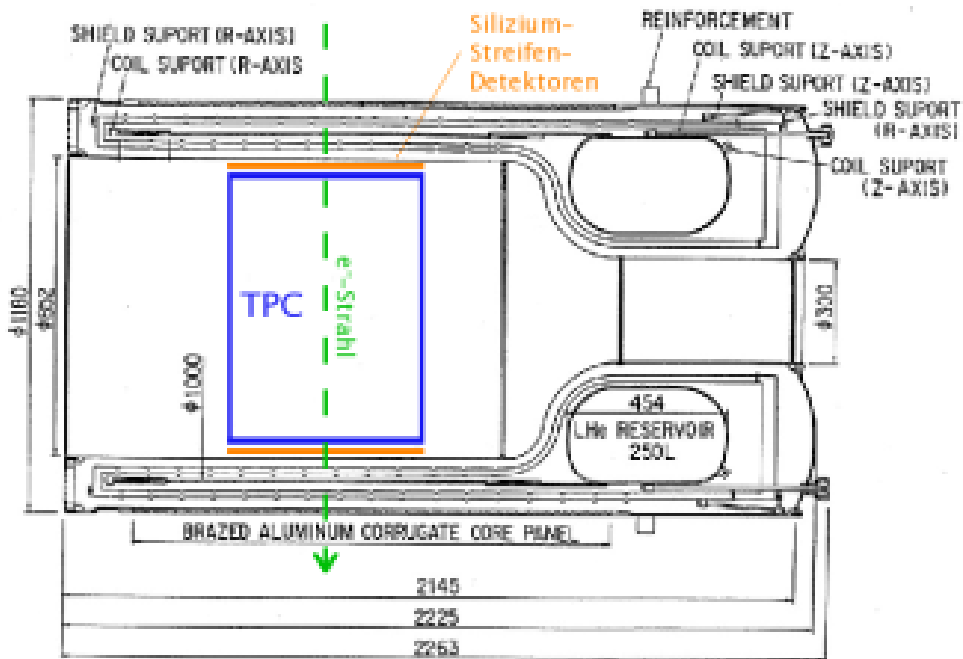


Figure 6: A technical drawing of the superconducting magnet (PCMAG) with the TPC indicated

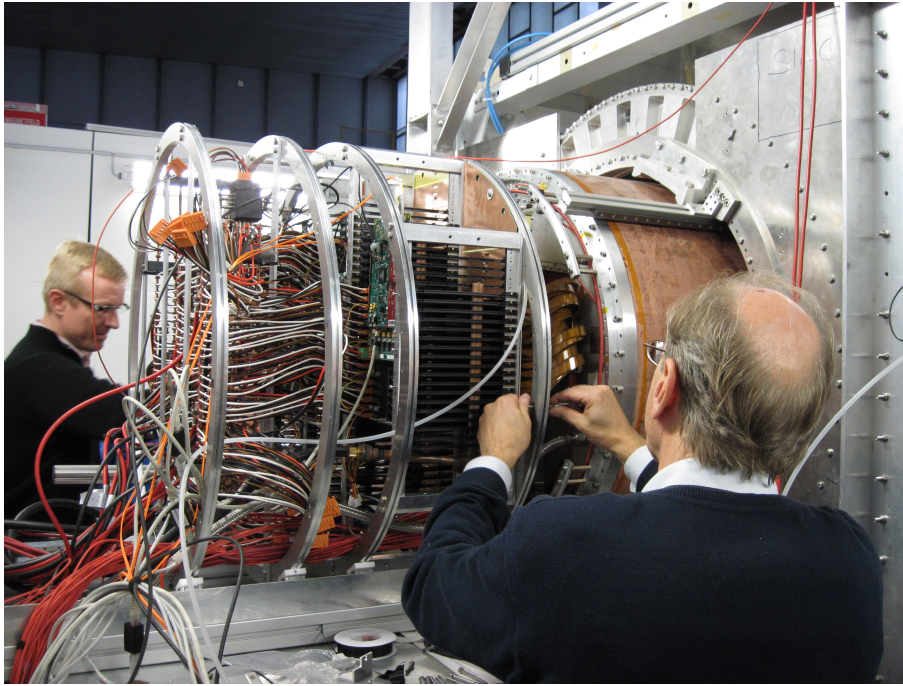


Figure 7: The front end electronics and its support structure attached to the TPC. Also seen are the optical cables for the data readout and the LV supply cables.

board. They are connected to the pad board on the TPC via flexible 30 *cm* long kapton cables. A Readout Control Unit (RCU) [13] governs the readout of the data via the back-plane to which a maximum of 32 FECs can be inserted. Data are sent via an optical cable to a Detector Read-Out Receiver Card (DRORC), which is placed in the Data Acquisition (DAQ) PC. The DAQ software uses the ALICE drivers and libraries for communication between the DRORC and the front end electronics via the optical link. At the reception of the trigger the ALTRO starts storing digitised information in the event buffer, up to a predefined number of samples. The RCU reads the ALTRO event buffer and sends the data on the optical link to the DRORC, which stores it in the memory of the readout computer. The events are stored on a local disk, a fraction of the events are sent to a monitoring program. A photograph of the test beam set-up is shown in Fig. 7.

The electronics pedestal and noise levels for all readout channels have been measured both initially as well as on a regular basis during data taking periods, mainly for pedestal subtraction and to check whether there are corrupt channels. The front end electronics has shown excellent noise performance, with a noise level of 0.5 ADC counts corresponding to an equivalent noise of 260 electrons for the longest shaping time and the lowest gain, where the noise includes random noise, coherent clock noise and long term variations on the scale of seconds. If the gain is increased to the highest value (27 mV/fC) the noise level increases to typically about 1 ADC count, which corresponds to the equivalent noise of 231 electrons at this gain.

## 7 Measurement principle

The first purpose of the test beam was to assess the performance of the LCTPC setup described above. In addition, this setup gave the opportunity to follow up on a study performed on the ALICE TPC using a detailed low level simulation of the detector [14].

The input to these simulations is the energy loss of the charged particle in the chamber gas, obtained from photo absorption ionization (PAI) models [15, 16, 17]. However, an accurate simulation also needs a very good description of the detector effects, such as diffusion, gain amplification variations, and pad response function coupling to different pads/rows. When energy loss calculations are combined with detector effects a good quantitative agreement can be obtained with data, see Fig. 8

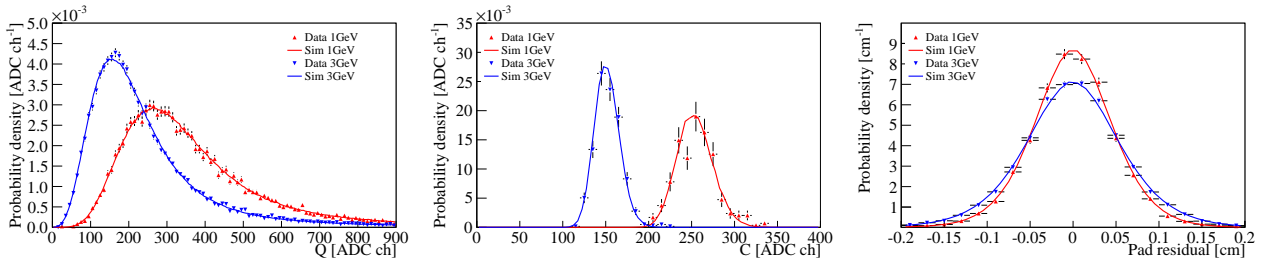


Figure 8: Comparison of simulated data to ALICE TPC test beam data (1 and 3 GeV/c protons) for the straggling function (left), truncated mean ( $dE/dx$ ) (middle) and position resolution (right). Figures are from [14].

For these studies test beam data is of great importance because there the beam geometry is fixed so that one gather data/statistics under essentially the same conditions (diffusion, track angles etc.) and the identity of the beam particles is well known.

The PAI model calculations include atomic shell effects, but these are hard to observe in the data, because typically the pad length is much larger than the mean free path so that one collects the ionization electrons from several collisions smearing out the discrete energies. For this reason a measurement was performed with the LCTPC rotated by 90 degrees with respect to the test beam so that the short side of the pad (1.2 mm) was parallel to the beam direction whereas the long side (5.2 mm) was transverse to the beam direction. These runs take advantage of the fact that the GEM readout, unlike wire readouts, have no preference for track angles (this is of course not true for the pads but as we want to focus on the energy loss in these runs the worsened space point resolution is not a problem).

Using this configuration, we try to get insight on the energy loss process, in particular on the shell effects present in the PAI model.

This approach using low level simulation presents other advantages:

- It provides the basis for simulation that anyway has to be developed for a detector.
- It enables a cross check whether the measured performance is optimal or could be improved?
- It allows for calibration of the energy loss. The gain can be obtained from the matching of simulation and data.
- It fixes parameters for particle identification using the specific energy loss: mean, resolution, and shape of curve.

## 8 Simulation

For this study an independent TPC simulation program developed in Lund for a study of the ALICE TPC [14] has been used. The simulation has proven to give a good description of test beam data with the ALICE TPC. For the LCTPC, only the readout part was modified to describe GEMs instead of wire chambers. The processes describing the ionization of the primary particle and the diffusion in the drift volume are the same. The gas processes are:

1. The mean free path is used to randomly determine the distance to the next primary interaction.
2. The particle is propagated to the point of the interaction and an energy loss,  $E$ , is randomly determined from the model distribution.
3. The energy loss is converted into a total number of ionization electrons,  $N_e$ , using the expression:

$$N_e = \frac{E - I}{W} + 1, \quad (1)$$

where  $I = 15$  eV is the first ionization potential, and  $W = 25$  eV is the effective energy required to create an electron-ion pair. These values were evaluated from the data in [18]<sup>1</sup>.

4. Each electron is individually propagated to the pad plane of the readout chamber taking into account only the diffusion. The diffusion constants used were the ones measured with the prototype during the run corresponding to this study.

The simulation of the GEM readout for each drifting electron includes the following processes:

5. At the Gem plane, the electron is assigned a random gain, following an approximate Polya function with factor 1.5.
6. The charge is transferred to the pad plane according to a two dimensional pad response function (PRF). A simple gaussian model is used. Alternative models were tested, but did not seem to induce any change in the results. The width of the PRF was determined from the data. The pad geometry used is exactly the same as used for the data reconstruction.
7. Steps 1-6 are repeated until the particle leaves the active volume.
8. Background noise is added. On top of a random gaussian noise, we add cross-talk in cables. A signal is induced in neighbouring wires in the cables from the pads to the front end card. This effect has been studied from the test beam data itself, as shown in section 10, and the amount of cross-talk was tuned to these results.
9. The data is reconstructed using the same program as for the real data.

The parameters for the energy loss in the gas are directly taken from the models, without any tuning. The parameters specific to the chamber such as the drift velocity, diffusion constant, PRF width and crosstalk were all obtained from different measurements on the test beam data. The only free parameter used to tune the simulation is the absolute value of the gain. It is hard to disentangle the amplification gain from the mean number of primary electrons, and therefore the constraints on the energy loss model are difficult to quantify.

---

<sup>1</sup>This means that  $N_e = 1$  for  $E \leq I + W$ ,  $N_e = 2$  for  $I + W < E \leq I + 2W$ , and so on. In the case of PAI models one can have energy losses,  $E < I$ . This always results in 1 electron in our simulation.

# 9 Track reconstruction and track selection

## 9.1 Geometry

In the parallel configuration (standard running configuration), the pad plane is oriented with the long side of the pads parallel to the beam direction. The coordinate system used in the reconstruction defines the  $z$ -direction parallel to the drift direction with the origin at the pad plane, pointing towards the inner of the TPC. The  $x$ -direction is oriented perpendicular to the pad rows (along the long side of the pads) and the  $y$ -direction is accordingly parallel to the pad rows (along the short side of the pads). A sketch of the pad layout with a track signal, and the coordinate system can be found in Fig. 9.

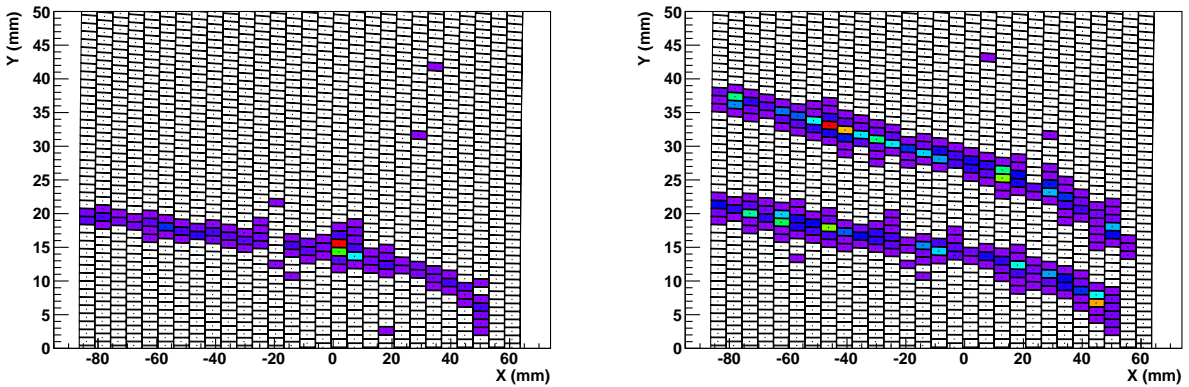


Figure 9: Display of events with one and two tracks, respectively, with the TPC in the parallel configuration. The coordinates of our reference system are also given.

## 9.2 Clustering

The first step of the *clustering* procedure is to reconstruct the pulses collected on individual pads. The charge collected on the pads is sampled at a frequency of 20 MHz and converted to digital information. Thus, the raw data contains the sampled ADC values, channel number and time information of such pulses (fig. 10). A pulse is defined by the hardware as two or more consecutive nonzero samples, where the threshold is set to 3 ADC counts. The largest ADC-value  $Q_{max}$  represents the pulse height and is chosen as a measure of the charge. Time information is retrieved by a charge weighted mean of the five samples around the peak of the pulse. The coordinates of the pulse is taken as the coordinates of the pad center on which the charge was deposited.

Two charge clouds close in time and space might accidentally be included in the same pulse, for example when two tracks pass close to each other. To split them, the algorithm compares the heights of all samples included in a pulse. Starting from one end, a peak is found when the value of a sample is lower than the preceding one. A difference of a two ADC values is required to avoid false peaks resulting from noise fluctuations. All samples up to the point where the values start rising again are included in the first pulse. For the values after that, the procedure is repeated should there be more than two pulses.

The reconstructed pulses are used in an algorithm that combines the pulses in a single pad row into clusters. A search is conducted outwards from the pad having the highest charge. If a pulse is found on a neighbouring pad, within a time window around the peak value, it is added to the cluster. The

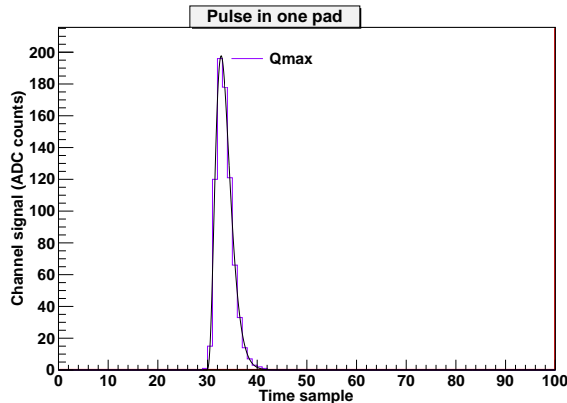


Figure 10: Typical pulse from sampling on an individual pad.

search continues until an empty pad or the end of the pad row is reached. At this point, the search algorithm stops and the pulses are flagged as used to allow the algorithm to find the remaining clusters in the row.

The  $x$  and  $y$  coordinates of a cluster are calculated from the coordinates of the center of the individual pads. Using a center of gravity method, the cluster coordinate  $y$  for example, is calculated according to

$$y = \frac{\sum y_i Q_i}{\sum Q_i} \quad (2)$$

where  $y_i$  denotes the  $y$ -coordinate of the pad  $i$  and  $Q_i$  is the charge deposited in this pad. The same method is also applied to the  $x$  and  $z$  coordinates, where in the case of  $z$  the coordinate can be obtained from the time information of the pulse and the drift velocity of the electrons in the chamber gas. The total charge of the cluster is calculated as the sum over the individual charges of the included pulses.

Thanks to the low amount of noise present, it is not necessary to perform any cuts on the clusters. After tracking has been performed, cuts on e.g. cluster size has a very small effect.

### 9.3 Tracking

For track finding, a simple algorithm is used that performs well in the low track density and low noise environment. A cluster at the module edge is chosen as a starting point. Since the pad plane, in the parallel configuration, is oriented with the beam along the long side ( $x$ -direction) of the pads, the next cluster in the track should be found in the neighbouring pad row. A search window is therefore defined around the start cluster in the drift direction ( $z$ -direction) as well as in the  $y$ -direction. If a cluster is found within the  $y - z$ -window in the next pad row, it is added to the track. If no cluster is found, the search continues in the next row. Here, a cluster must be found or the track candidate is rejected so that a track is not allowed to contain holes larger than one row. If more than one cluster is found, the one lying closest to the previous cluster in  $y$  is chosen.

The procedure is repeated with a new search window around the previous cluster until the other module edge is reached. In order to be accepted, a track needs to include at least 10 clusters and no more than two empty pad rows. The algorithm has been tested extensively and visual cross checks have confirmed that it works well.

When a track has been found, the clusters in it are flagged so that the algorithm can be run again over the remaining clusters. This allows for multiple tracks to be found. Due to conversion, multiple

track events do occur and it is important to find them since they will have an effect on the energy loss distribution.

In the end of the tracking procedure, a fit is made to the coordinates of the clusters. The straight tracks in the runs without magnetic field are fitted with a first order polynomial and the helical tracks with magnetic field are fitted with a second order polynomial.

## 9.4 Track Selection

In order to have good quality tracks, two conditions had to be fulfilled for inclusion of a track in the analysis. As mentioned, a maximum number of two missing pad rows were allowed so that the track must have clusters in all but at most two rows. In addition, the track is required to go through the middle of the module to avoid edge effects such as poorly reconstructed clusters where some of the charge ends up outside the instrumented region.

## 9.5 Perpendicular configuration

As explained in section 7, the LCTPC was also operated in a  $90^\circ$  rotated configuration. In this configuration the beam was perpendicular to the long edge of the pads and, thus, the width of the charge distribution collected on the pads should be compared to the length ( $5.2\text{ mm}$ ) of the pads. Due to the fact that the width of the charge distribution is smaller than the length of the pads the space resolution is very poor and does not allow to perform a conventional tracking. The track selection is done with the following method:

First a “clean” area is selected, far from the edges and dead regions of the module. Two “trigger” regions were defined (see fig. 11), which should contain hits to indicate the occurrence of a possible track. From the signal in these two regions, a virtual track was formed. The pulses within two pads on each side of this line (in the  $x$ -direction) will contribute to the reconstruction of the real track.

On the signal in the corresponding region in  $x - y$ , we apply the same kind of clustering as in the parallel configuration. Instead of a pad row, we cluster along a “pad line” which connects each pad to one of its two neighbours in the next row.

The tracks defined have at most 52 clusters (see fig. 11).

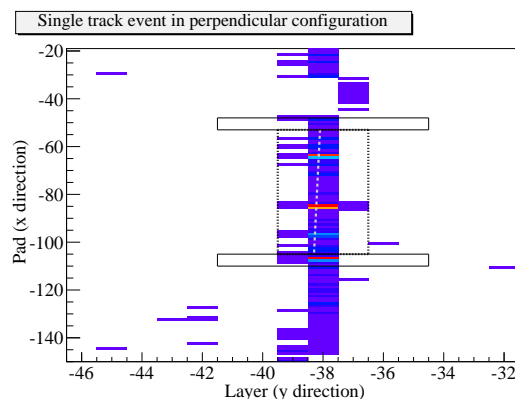


Figure 11: Display of an event with one track in the perpendicular configuration. The black rectangle represent the trigger regions. The gray dashed line is the virtual track. The fine dashed box shows the pads included in the track.

## 9.6 Event selection

For the following analysis, pure samples of 5  $GeV/c$  electron tracks with the most stable conditions possible were selected, rejecting events with the following two problems:

**Gain drops** It was observed that a few times per run, the overall gain dropped. From a fit to the average charge of consecutive events in the low gain regions, the gain drops could be identified. Using this, we clean up the data by cutting out the low gain events as shown on Fig. 12.

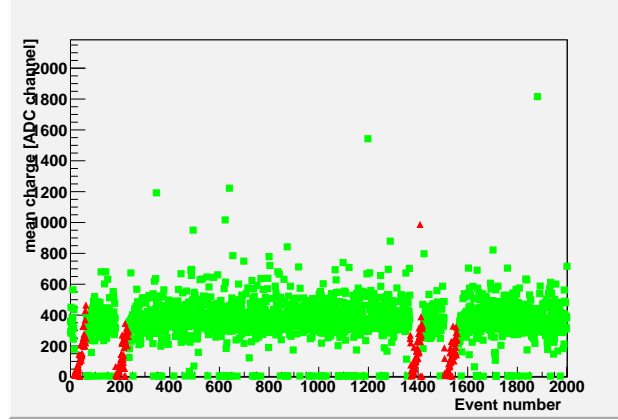


Figure 12: Average pad charge in each event for one run. Periods with gain drop (red triangles) are rejected. The events with zero charge are empty (fake trigger).

**Multiple tracks** To avoid events with multiple tracks in the perpendicular configuration, events where the ratio between the signal inside and outside a track is too high are rejected (the threshold is tuned for each run).

In both configurations, a cut on the  $dE/dx$  of the track is also done to remove double tracks which are too close to be separated in space and time. These look like single track, but has a  $dE/dx$  twice as large.

## 10 Cross talk

In the perpendicular run configuration, the width of the charge distribution from the track is smaller than the width of a pad row ( $5.2\text{ mm}$ ), so that most of the time, we only get signal in one or two pad rows. This fact will be used to measure the signal induced in neighbouring channels through crosstalk in the kapton cables between the pads and the FEC.

### 10.1 Track selection

First, tracks are defined and selected as explained in section 9.5. From this track sample a refined selection is done to have only tracks that approximately follows the border between two pad rows (in the  $y$ -direction). Since the pad geometry is somewhat curved, and the tracks are bent in the magnetic field, a track can in practice never fulfill this requirement exactly and the poor space resolution in the perpendicular configuration does not allow a very precise reconstruction and selection of the proper tracks. However, different approximate methods of selection were tried and they all gave the same final results.

The tracks obtained are separated into two categories (see Fig. 13):

**A** tracks going between pad rows connected to different connectors

**B** tracks going between pad rows connected to the same connector

In Fig. 13, the definition of the “close” and “away” rows are given, corresponding to the two rows closest to the track, and their neighbours, respectively. Since the track is going along the border of two pad rows the charge should give signals in the pads of both “close” rows, whereas it is not expected to see any signal in the “away” rows due to the electron cloud being much smaller than the pad size transverse to the track in this configuration. This can be verified by events from the case B where no signal should be observed on the “away” rows since these are read out by different connectors compared to the “close” rows and therefore could also not have any contribution from possible cross talk in the cables. For events fulfilling the requirements of case A the “close” rows are read out by different cables and the only explanation for an observed signal in the “away” rows must be cross talk in the kapton cable.

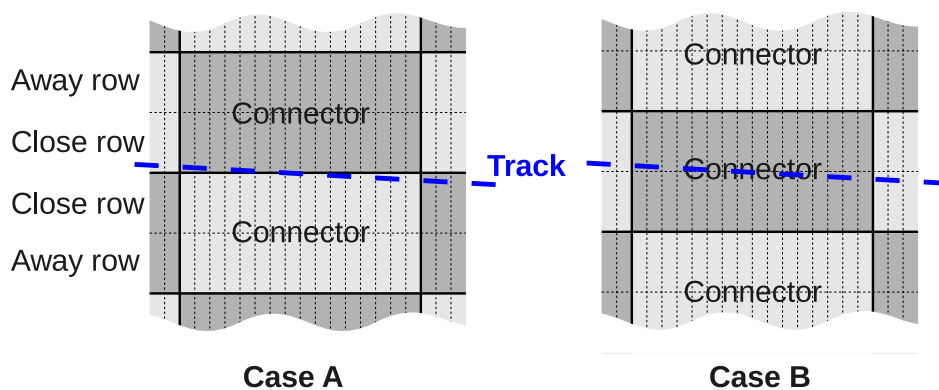


Figure 13: Schematic picture giving the definition of the “close” and “away” rows, respectively, for the two situations A and B described in the text.

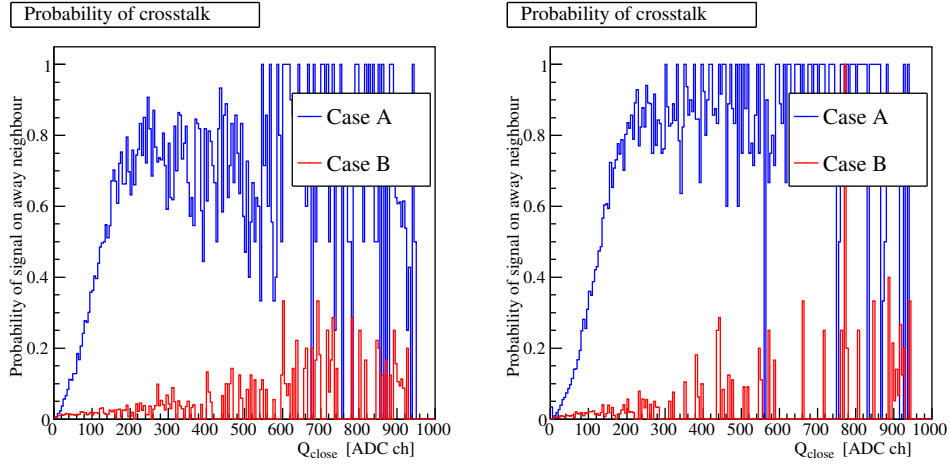


Figure 14: Probability to observe a signal in the “away” row, when a signal on the “close” row is measured. The left and right plots correspond to the pad rows on each side of the track.

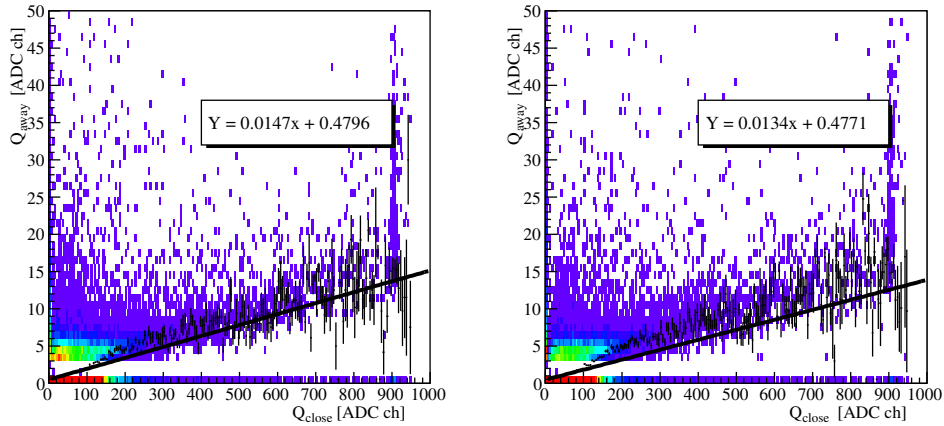


Figure 15: The charge deposited on pads in the “away” row versus that deposited in the “close” row for case A. The left and right plots show the distribution for the two neighbouring channels in the cable.

## 10.2 Results

The first goal was to see whether the results gave any indication of cross-talk. Fig. 14 shows the probability to get a signal in the “away” row, when there is one in the “close” row. It is clearly seen that in case A, if the “close” signal is large enough, there is almost always an “away” signal, while in case B, a signal almost never appears in the “away” row (as expected since these are read out by different cables). Exactly the same effect is observed for the pad rows on each side of the track, which excludes the possibility of a geometric effect from the track angle or the curved pad geometry.

The cross-talk results shown in Fig. 14 suggest a threshold effect around  $Q=200$  ADC counts. In Fig. 15, the charge collected on a pad in the “close” row is plotted versus the charge collected on its neighbouring pad in the “away” row for the case A. Here the neighbour pad is chosen specifically to be one of the two closest cable lines in the readout cable. From this figure we see clearly the effect of zero-suppression for the low charges, for which the cross-talk is mostly below threshold. From the fit on the average correlation in Fig. 15, it can clearly be seen that the effect of the cross-talk is below 2% of the main signal. The results were confirmed by doing a test with a pulse generator.

# 11 Performance study

The data taken with the LCTPC in the two different configurations described above were analysed and compared to the results from simulations. The simulated data was created with the same format as real data. The analysis of real and simulated data were performed in exactly the same way, using the clustering and track finding as described in section 9.

## 11.1 Charge deposition

The main focus was on the charge deposition and the purpose was to confront the energy loss models with data. Since the absolute signal gain was the only free parameter of the simulation, it was important to match it to the data.

### 11.1.1 $dE/dx$ resolution

In order to determine the gain in the simulation, the  $dE/dx$  of the tracks was measured. Since we use ultra-relativistic electrons, on the plateau region of the Bethe-Bloch curve, a very clean sample for the  $dE/dx$  is expected. The value of  $dE/dx$  is calculated as the 60% truncated mean of the signal in the track, taking the mean of the 60% lowest signals in the track.

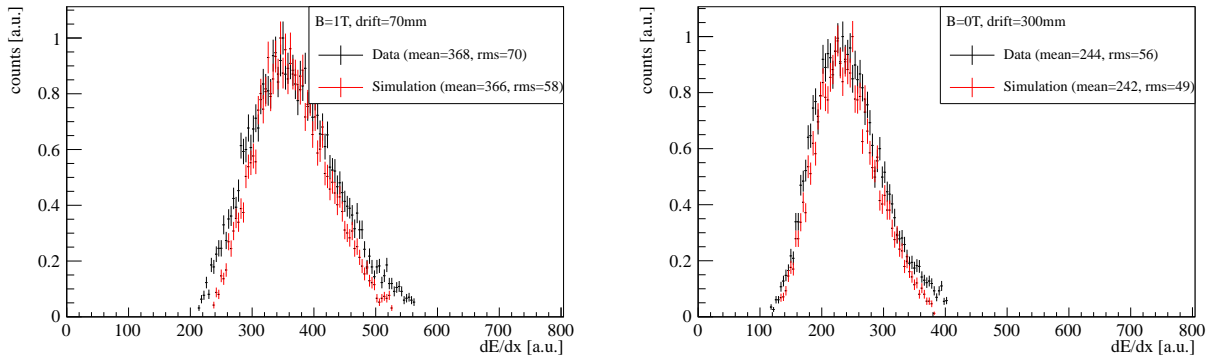


Figure 16: The  $dE/dx$  spectrum, calculated from the 60% truncated mean. A comparison between simulation (in red), using Geant4's PAI model, and data (in black) is given in the case of a 1 T magnetic field (left) and no magnetic field (right).

The results are shown for the parallel configuration in Figs. 16 and 17. The gain parameter in the simulation is adjusted so that the mean value of the  $dE/dx$  distribution agrees with the experimental data. It can be observed that the  $dE/dx$  distribution in the simulation is somewhat narrower than that of the real data.

In Fig. 17, we see that the diffusion gets more prominent as the drift distances increase, an effect that is especially significant with no magnetic field and less significant with a 1 T magnetic field on. The correlations that the diffusion induces between pad rows (i.e. between clusters in the track) alters the charge distribution and worsens the  $dE/dx$  resolution.

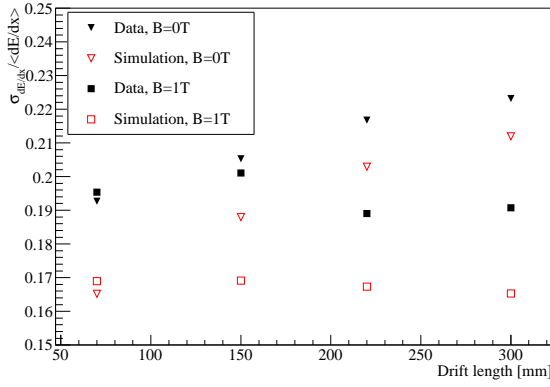


Figure 17:  $dE/dx$  resolution as a function of drift distance.

### 11.1.2 Charge distribution

To get a better understanding of the  $dE/dx$  results, the full charge distribution of the clusters in the tracks can be studied. The results are shown in Fig. 18. It can be observed that the simulation does not describe the data taken in the parallel configuration very well. The energy loss model is not precise enough to reproduce the details of the data. However, when the diffusion increases as is the case with no magnetic field and longer drift lengths, the correlations between clusters smear out the details of the model, and simulation and data start to agree.

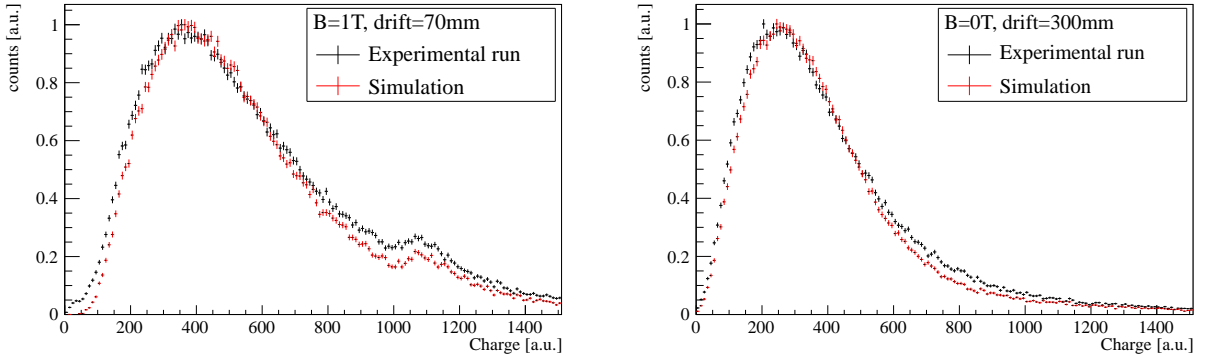


Figure 18: Charge distribution in different diffusion cases (left: minimum diffusion (short drift,  $B=1T$ ), right: maximum diffusion (long drift,  $B=0T$ ). With increasing diffusion, the details of the energy loss model are smeared out and the simulation gives a better description of the data. The bumps in the low diffusion case is caused by the saturation in ADC channel 1024 of the digital signal in each pad (see section 6).

### 11.1.3 Comparison of the charge distributions for the two configuration

With the two configurations (parallel and perpendicular), we have the opportunity to test the consistency of the energy deposition comparing sampling over short track segments ( $1.2\text{ mm}$ ) and longer ones ( $5.2\text{ mm}$ ). Due to different levels of correlations, the charge distribution does not scale in a simple way as the sampling length is increased [16]. However, since the size of a pad is approximately  $1.2\text{ mm}$  by  $5.2\text{ mm}$ , the width of four pads is  $4.8\text{ mm}$  which is approximately the same as the length of a pad. Thus, by combining signals from 4 neighbouring pads in the perpendicular configuration, the charge distribution should be comparable to that of the parallel configuration.

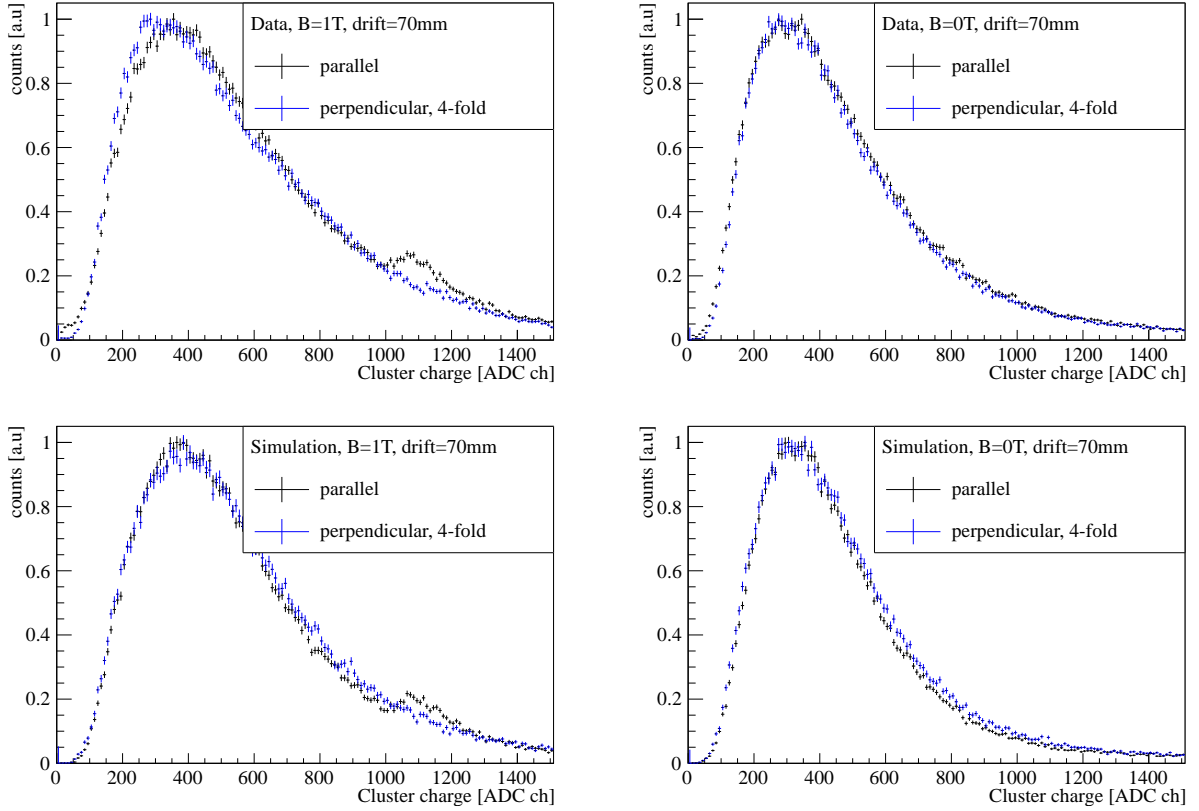


Figure 19: Comparison between the charge distribution for the parallel configuration (5.2 mm long pads) and the charge collected on four consecutive pads (4x1.2 mm) in the perpendicular configuration. A correction factor is introduced to compensate for gain difference and possible efficiency difference. The upper plots are data and the lower are simulation with the same run characteristics.

In Fig. 19, the charge distribution from track clusters in the parallel configuration, is compared to the charge distribution of clusters grouped over four consecutive pads in a track in the perpendicular configuration. The conditions for the runs which are compared are the same i.e. the drifts length, magnetic field, electronics settings are identical. An additional scaling of the charge is done for one of the configurations to account for gain variations and possible different charge collection efficiencies.

Fig. 19 gives comparisons of charge distributions for the two different configurations with (left hand plots) and without (right hand plots) the magnetic field on, for real data (upper plots) and for simulation data (lower plots). The agreement is perfect. In spite of the differences in the charge distribution (fig. 18), it is clear that the simulation reproduces the consistency between the two configurations. This indicates that besides the energy loss process, the detector is well described by the simulation. It also means that effects observed on the charge in the perpendicular configuration should be consistent with what is observed in the parallel configuration.

#### 11.1.4 Perpendicular configuration

The final step of the energy loss study was to investigate if it was possible to observe the details of the energy loss process from measurements in the perpendicular configuration with a 1 mm sampling length. In Fig. 18 it was noticed that there are discrepancies between the real and the simulated data for the parallel configuration. However, in section 11.1.3, it was shown that measurements in the two configurations are consistent. Thus, the discrepancies observed in the measurements with the

parallel configuration could be further investigated in the perpendicular configuration and possibly be associated with some details of the energy loss model.

In Fig. 20 the charge distribution for different steps in the simulation are shown for the lower part of the pulse height spectrum. A description of the various distributions is given below:

**Number of ionisation electrons** , represented with triangle ( $\blacktriangledown$ ), is the number of electrons produced after ionisation, at the track level, over the longitudinal size of the pad (1.2 mm). For comparison, it is multiplied by the average gain.

**Number of electrons reaching the GEMs** , represented with blue squares, is the number of electrons reaching the GEM plane. The only added effect from the previous number is diffusion. For comparison, it is multiplied by the average gain.

**Reconstructed charge** , in red open circles, is the charge read out on the pads, after all effects (gain variation, noise, digitisation). It is the value to be compared directly to the data (represented with the black circles).

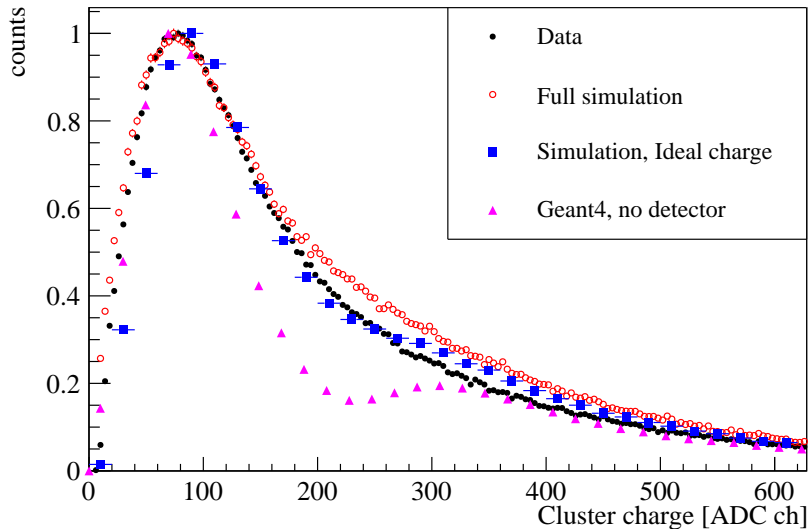


Figure 20: Charge distribution for minimum diffusion, with 1.2 mm wide pads for the lower part of the pulse height spectrum. The triangles ( $\blacktriangledown$ ) show the number of ionisation electrons produced. The blue squares shows the number of electrons reaching the GEM plane (after diffusion). The red open circles is the full simulation. The real data is represented by black full circles. We can see the bump from the second shell of Argon can be associated with the excess the simulation shows compared to data around 300 ADC.

In Fig. 20, a bump in the number of ionisation electrons (around 300 equivalent ADC channels) is observed, which is related to the L shell in Argon. Following the steps in the simulation shown in the figure, we can associate this bump to an excess in the reconstructed charge compared to data around 300 ADC channels. This suggests that the ionization from inner shells is inadequately modeled.

## 11.2 Space Resolution

Since no external reference is available, the resolution is calculated with respect to the reconstructed track. The track is obtained from a fit to the cluster coordinates and the residuals (in  $y$ ) of the individual points are calculated using this fit. The resolution is then obtained as the width  $\sigma_y$  of the residual distribution, obtained from a gaussian fit. Since the investigated point is included in the fit,

this is expected to give an estimation that is better than the actual resolution. A common approach to this is to use the Geometric Mean method. According to this method, another fit is made, this time excluding the investigated point. The geometric mean of the resolutions obtained with the two methods is then calculated  $\sigma = \sqrt{\sigma_{in} \cdot \sigma_{ex}}$ , where  $\sigma_{in}$  and  $\sigma_{ex}$  is the resolution calculated with the point included and excluded, respectively, in the fitting procedure. This is considered to be a more reliable estimation of the “true” resolution.

Without magnetic field (Fig. 21), the simulation gives a perfect description of the space resolution in the data.

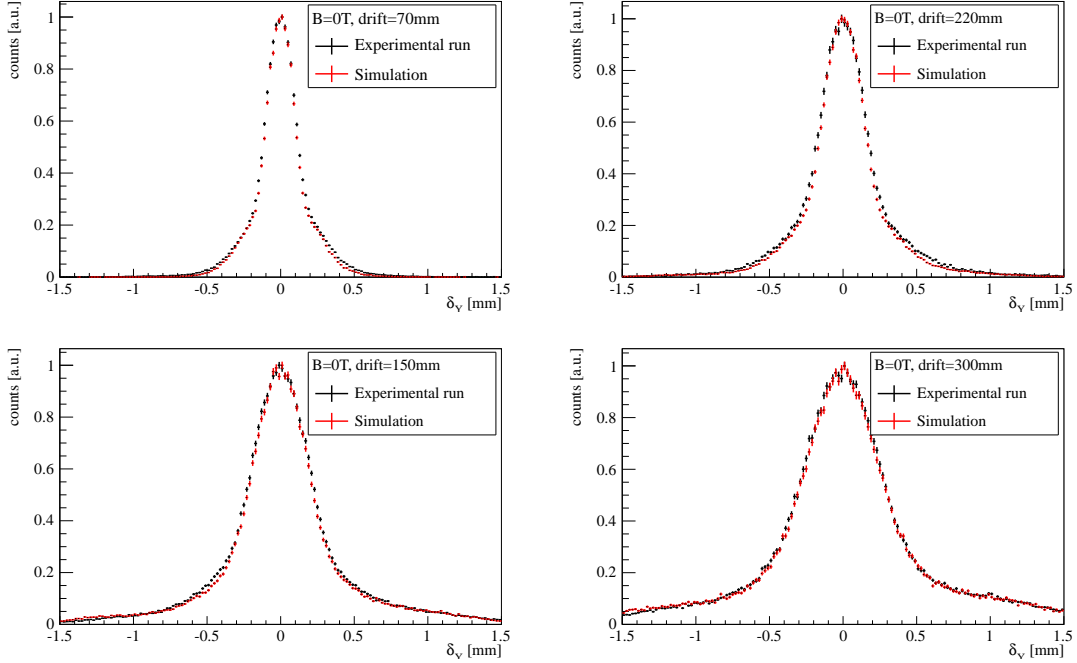


Figure 21: Space residuals for different drift distances, without magnetic field. The simulation (in red) gives a perfect description of the data.

As mentioned in section 4, there was an inhomogeneity of the electric field around the edges of the GEM plane. In the presence of magnetic field, this caused distortions of the tracks, due to the  $E \times B$  effect. The tracks appeared as a consequence of this slightly deformed compared to the expected arc. This worsened considerably the resolution measurement relying on a polynomial fit to the track.

An attempt to correct for the distortion was made, using the residual distributions of the individual pad rows. The residuals are calculated assuming a helical track described by a second order polynomial in the transverse projection. Due to the known problem with the distorted electric field at the edges of the GEM the information from outermost 5 pad rows were excluded and a fit was only performed for the middle part of the track, which should be less influenced by the field inhomogeneities. Fig. 22 shows the calculated residuals versus the pad rows for many events in a run. A clear S-shape can be observed. Taking the residuals averaged for each row (x-value) a distortion (y-value) can be calculated. This averaged value is used to correct the  $y$ -coordinates on a row-by-row basis.

To account for the distortion in the simulation, a fit with a fifth order polynomial to the distortion shape in the data was made as shown on Fig. 22. The fitted distortion was included in the simulation as follows. Since the position of the clusters in the  $x$ -direction cannot be measured to a better precision than the length of the pads (5.2 mm), the displacement (in the  $y$  direction) applied to each cluster was chosen from the fit at a *random* point (in the  $x$  direction) in the corresponding pad row. When the simulated data are corrected in the same way as the real data by the distortion (now *average* over

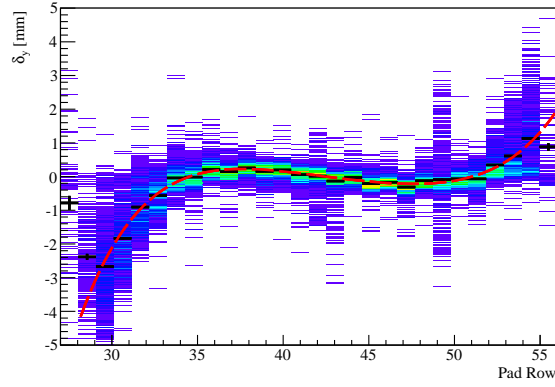


Figure 22: Space residuals  $\delta_y$  versus pad row. The S-like shape is a consequence of the  $E \times B$  effects associated with electric field distortions caused by the support pillars of the GEMs. This profile (black lines) is used to correct the data. The profile is fitted (dashed line) to provide a model of the distortion for the simulation.

the pad length), a spread of the residuals in each row remains due to the unknown cluster position along the pad length. Fig. 23 shows that the simulation gives a good description of the data after inclusion of the track distortion. Ideally the distortions should be done at the electron level in the simulation, but these results anyway suggest that the origin is our lack of knowledge of where along the pad the electrons dominates. Therefore this distortion cannot easily be corrected for, and, to achieve the resolution of  $70 \mu m$  predicted by the simulation, the electric field close to the GEMs has to be improved.

The space resolution ( $\sigma_y$ ) for different drift distances are shown in Fig. 24 from which it is seen that when the drift distance, and therefore the diffusion, is increased, the resolution of the space position of the track becomes worse.

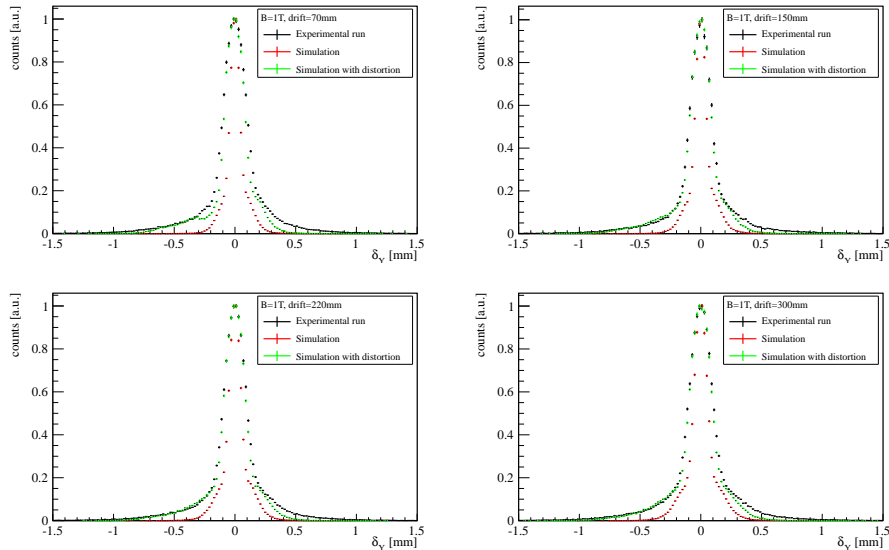


Figure 23: Space residuals ( $\delta_y$ ) for different drift distances, with magnetic field. The  $E \times B$  effects, associated to the electric field distortions caused by the support pillars of the GEMs, made the resolution worse for the data (black) than for the simulation (red). After introducing corrections to account for the distortions, the simulation (in green) gives a much better description of the data.

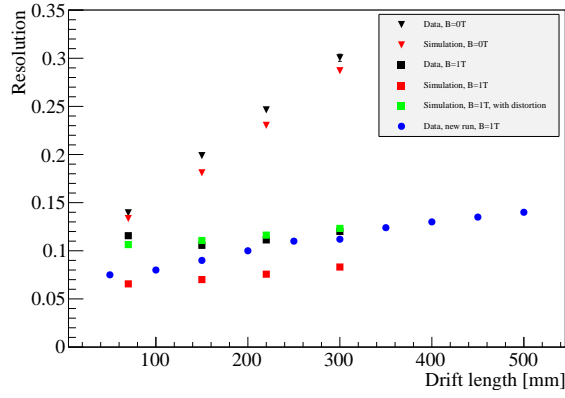


Figure 24: Space resolution for data and simulation. When the drift distance, and therefore the diffusion, is increased, the resolution of the space position of the track becomes worse. With magnetic field,  $E \times B$  effects associated with electric field distortions made the resolution worse for the data (black squares) than for the simulation (red squares). After including the distortion, the simulation (green squares) matches the data.

The blue dots show for comparison the resolution measured by the Japanese group on more recent data using the same setup. The method of calculation was different, which explains the slightly different values.

### 11.3 Influence of ADC resolution

In the current version of the electronics, the analogue signal is digitised with a 10-bit precision (1024 ADC channels). This high resolution is likely to be better than needed, given that the pad width is only 1.2 mm. Reducing the ADC resolution to an optimal value will result in a reduction of power and cost for the electronics.

In order to test this, the digital representation of the raw signal was changed by removing the ADC bits one by one to see at which point a decrease in resolution could be observed. The regular reconstruction is then performed. The size of the ADC signal is reduced from 10 bits down to 8, 6 and 4 bits, and the performance of the LCTPC is compared for the various resolutions.

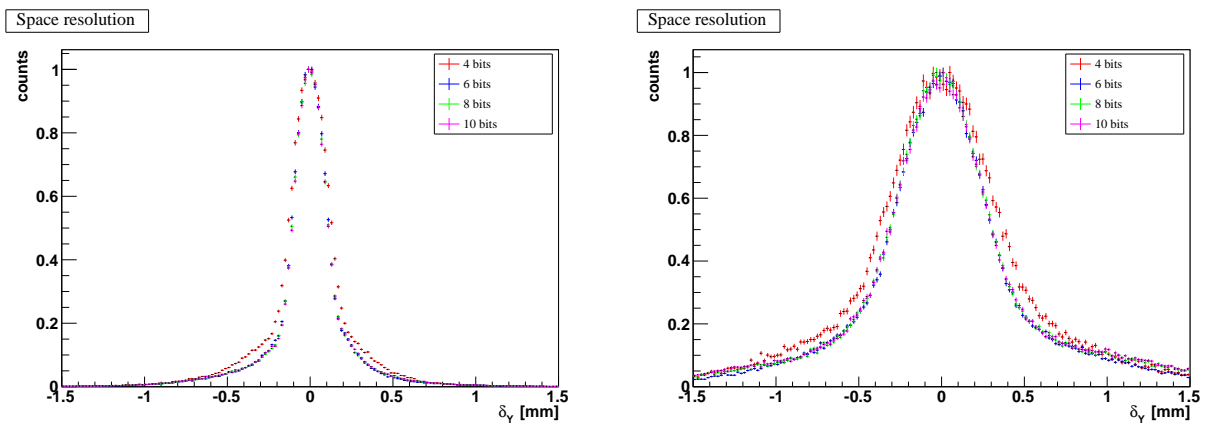


Figure 25: Examples of space residual ( $\delta_y$ ) distributions for different values of the ADC resolution. On the left, with minimum diffusion (70 mm drift and magnetic field on), and on the right with maximum diffusion (300 mm drift and no magnetic field).

From Figs. 25 and 26, it is obvious that no deterioration of the space resolution is observed until

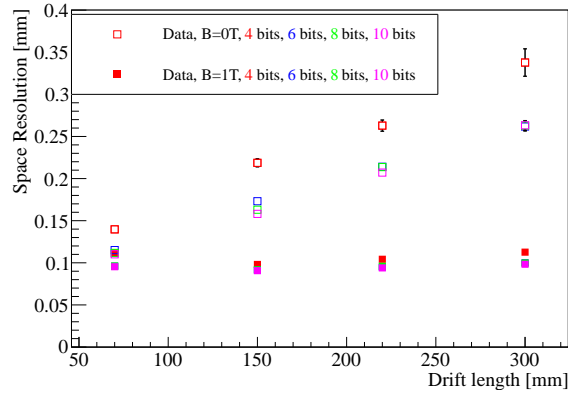


Figure 26: Space resolution as a function of drift distance for different values of the ADC resolution.

the precision has been lowered to 6 ADC bits. Below that a worse space resolution is observed, mostly because of threshold effects.

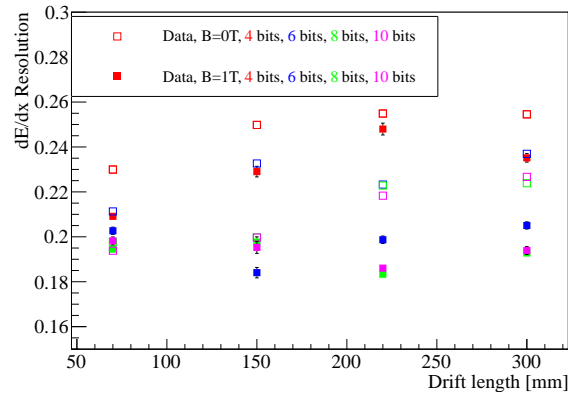


Figure 27:  $dE/dx$  resolution as a function of drift distance for different values of the ADC resolution.

In Fig. 27, it is seen that, as expected, the loss in ADC resolution has more influence on the  $dE/dx$  resolution. However, down to 6 bits, the loss is not excessive, and begins to be significant at 4 bits.

This shows that the ADC range can be reduced without real damage to the performance. However, this test has been done with electrons on the ultrarelativistic plateau. It should be confirmed for minimum ionising particles, where the effect should be maximal. There is in any case range for adjustment of the digital signal.

## 12 Conclusion

The large prototype TPC (LCTPC) equipped with Asian GEMs and electronics based on the ALICE ALTRO, has been successfully set up and tested thoroughly in the DESY T24 electron beam with different configurations. The data has been reconstructed, analysed and compared to simulations using software developed in Lund.

Running the LCTPC in a rotated configuration allowed to reach a high level of detail in the study of the charge distribution along tracks. The comparison to simulation allowed to probe the limits of the energy loss models, in particular the PAI model offered by GEANT4.

This unusual orientation also allowed to study cross talk in the readout cables in a real data taking situation.

In spite of imperfection of the energy loss model, the performance of the TPC has been very well described by the simulation. A loss of resolution from distortions from  $E \times B$  effect related to inhomogeneities of the electric field close to the GEM was observed. The observed resolution could be described by simulation with a simple correction in reconstructed clusters to include the distortions. While it shows that there is little hope to recover space resolution with the inhomogeneous electric field, it indicates that the resolution of  $70 \mu m$  shown by the simulation should be achievable if the field is improved.

## Acknowledgements

This work is supported by the Commission of the European Communities under the 6th Framework Programme "Structuring the European Research Area", contract number RII3-026126. The project was also supported by the Swedish Natural Science Research Council. We would like to thank K. Dehmelt, T. Matsuda and H. Kuroiwa for help in setting up the equipment needed for the measurement, and H. Bichsel and V. Grichine for help with the energy loss models for the simulation.

## References

- [1] T. Behnke *et al.*, EUDET-Memo-2007-11.
- [2] J. Timmermans, private communication.
- [3] T. Behnke *et al.*, EUDET-Memo-2006-042
- [4] T. Behnke *et al.*, "A Lightweight Field Cage for a Large TPC Prototype for the ILC", JINST **5** (2010) P10011 [arXiv:1006.3220 [physics.ins-det]].
- [5] K. Dehmelt on behalf of the LCTPC Collaboration, EUDET-Memo-2008-46
- [6] K. Dehmelt on behalf of the LCTPC Collaboration, EUDET-Memo-2009-9
- [7] A. Ishikawa *et al.*, "A GEM TPC End-Panel Pre-Prototype" *In the Proceedings of 2007 International Linear Collider Workshop (LCWS07 and ILC07), Hamburg, Germany, 30 May - 3 Jun 2007, pp TRK27* [arXiv:0710.0205 [physics.ins-det]].
- [8] T. Matsuda [LC-TPC Collaboration], "Results of the first beam test of a GEM TPC large prototype", JINST **5** (2010) P01010.

- [9] A. Yamamoto and Y. Makida, “Superconducting magnet for long duration flights”, Proceedings of the 5th Workshop on ‘Balloon-borne experiments with a superconducting magnet spectrometer’, KEK Japan, November 30 - December 1, 1994.
- [10] L. Musa *et al.*, “The ALICE TPC Front End Electronics”, Proc. of the IEEE Nuclear Science Symposium, 20 - 25 Oct 2003, Portland
- [11] R. Esteve Bosch, A. Jimenez de Parga, B. Mota and L. Musa, IEEE Trans. Nucl. Sci. **50** (2003) 2460.
- [12] L. Musa, “Prototype compact readout system”, EUDET-Memo-2009-31, 2009.
- [13] C. Gonzales Gutierrez *et al.*, “The Alice TPC Readout Control Unit”, *In the Proceeding of the 2005 IEEE Nuclear Science Symposium and Medical Imaging Conference, Puerto Rico, October 23-29, 2005*
- [14] P. Christiansen *et al.*, Nucl. Instr. and Meth. A 609 (2009), p. 149
- [15] J. Apostolakis *et al.*, Nucl. Instrum. Meth. A 453 (3): 597-605, 2000
- [16] H. Bichsel, Nucl. Instrum. Meth. A **562**, 154 (2006).
- [17] H. Bichsel, Nucl. Instrum. Meth. A **566**, 1 (2006).
- [18] ICRU Report 31: Average energy required to produce an ion pair. Bethesda, MD: ICRU Publications, 1979.